

Micro Coded-Aperture Lead-In of Light for Calibrating Remote Sensing Cameras

Jin Li^{ID} and Yuan Zhang

Abstract—We investigate the geometric calibration of a remote sensing camera using a micro coded-aperture lead-in (CAL) of light. A CAL can transform a light beam into multiple sub-beams with a precisely known diffraction angle. The multiple sub-beams can be considered as light sources of multiple point-targets at infinity. We experimentally confirm that this method can achieve an accuracy of approximately $101\text{ }\mu\text{m}$ and is simple to calibrate. This method has the potential to be used in the calibration of the interior parameters of optical remote sensors on the ground and in orbit.

Index Terms—Geometric calibration, micro coded-aperture lead-in of light, surface micromachining.

I. INTRODUCTION

HIGH accuracy image position determinations (IPD) of remote sensing cameras are crucial to observing targets on the ground [1]–[3]. In special cases, the in-orbit performance of a satellite depends primarily on the accuracy of the IPD. The positioning capability of these satellites is ensured mainly by the calibration of the intrinsic orientation parameters (IOPs) using a ground control point (GCP). Therefore, geometric calibration is a prerequisite for image positioning of a camera.

Remote sensing camera calibration includes two required stages: ground-based calibration and orbit-based calibration. Ground-based calibration results can be used for space mission planning and spacecraft design before launch. Orbit-based calibration usually corrects the variation in the ground-based calibration results based on the orbital working conditions after launch. Many camera calibration methods have been studied for ground-based calibration and orbit-based calibration [4], [5]. Our previous works proposed an in-orbit calibration method based on an auto-collimating dichroic filter in combination with a micro point-source focal plane (MPFP) [6]. This method integrates point light sources fabricated using a mask and bonds multiple light-emitting diodes (LEDs) to a complementary metal-oxide-semiconductor (CMOS) sensor in the camera focal plane. However, this method is not suitable for ground-based calibration because the MPFP cannot

Manuscript received August 3, 2017; revised September 9, 2017; accepted September 21, 2017. Date of publication September 26, 2017; date of current version October 25, 2017. This work was supported by the Natural Science Foundation of China under Grant 61505093. (Corresponding author: Jin Li.)

J. Li was with the Department of Precision Instrument, Tsinghua University, Beijing 100084, China. He is now with the Electrical Engineering Division, Department of Engineering, University of Cambridge, Cambridge CB3 0FA, U.K. (e-mail: hanj_lij@163.com).

Y. Zhang is with the Changchun Institute of Optics, Fine Mechanics and Physics, Chinese Academy of Science, Changchun 130033, China (e-mail: zhangyuanfresh@126.com).

Color versions of one or more of the figures in this letter are available online at <http://ieeexplore.ieee.org>.

Digital Object Identifier 10.1109/LPT.2017.2757010

produce the plane sub-wave required by an infinite target in on-ground calibration. Moreover, restricted in the number of LEDs, the point-sources cannot cover the full field of view (FOV) of a camera. A common ground-based approach for optical remote cameras is based on a single aperture or single pixel illumination in combination with multiple angle measurements [7], [8]. First, an uncalibrated remote sensing camera (URSC) is installed on a three-dimensional precision turntable. Then, a single aperture target (SAT), used as a grid target, is located on the focal plane of a collimator. Finally, an area source illuminates the SAT and is transformed into a collimated light by the optical system's collimator, which is captured by the uncalibrated remote sensing camera. When the turntable locates the position of different rotation angles, the URSC can obtain multiple positions of the single pixel point images from different FOVs. Finally, the center of the spot images at different FOVs is extracted by a centroid algorithm. Based on the radial distortion model of a camera, the distortion can be described by $\phi_i(f, \alpha_i)$, where i is one of the FOV positions, f is the principal distance, and α_i is the rotated angle. Based on the distortion theory of optical cameras, the total minimum distortion in the full FOV of a camera can be attained at the principal distance and principal point [9], [10]. To calculate the principal distance and principal point [11], a least squares method is applied to a geometric imaging equation, $\phi_i = x_i - (x_0 + f \cdot \tan \alpha_i)$, where x_i is the image's central point and x_0 is the principal point. However, the complicated calibration flow results in low efficiency because each imaging process can only capture a single image point of the two-dimensional (2D) FOV. Moreover, the vibration of the rotating turntable and the accuracy of the angle measurement also affect the calibration accuracy.

II. CALIBRATION WITH MICRO CAL

To overcome the above problem, we describe the use of a micro coded-aperture lead-in (MCAL) of light in calibrating the IOP of a camera. In an attempt to calibrate the IOP of a camera, the MCAL can transform a light beam into multiple sub-beams with precisely known diffraction angles. Fig. 1 sketches the calibration of the IOP of a camera with MCAL, where f_{camera} is the effective focal length, m is the diffraction order, θ_s is the separation angle between two focal spots, d is the distance between two focal spots, θ_f is the full angle, and D is the length of the spot array. The MCAL can transform a collimated input beam into several sub-beams with a predesigned separation angle and intensity, each with the characteristics of the original beam.

The phase distribution of MCAL is described by $\varphi(x, y)$. The distribution of the complex amplitude of the incident illumination on MCAL is represented by $u(x, y)$.

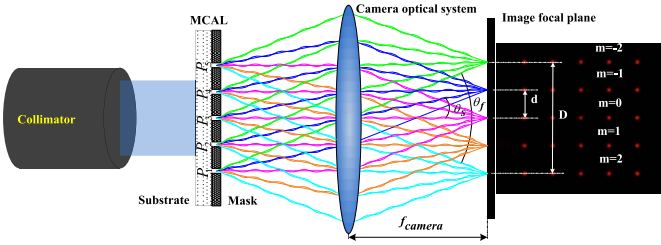


Fig. 1. Calibration of IOP of camera with MCAL.

The optical field output of MCAL can be expressed as $u_t(x, y) = u(x, y) \times \exp[i\varphi(x, y)]$, where $\exp(i\varphi(x, y))$ denotes the transmission function of MCAL. The diffraction field can be expressed as $U_t(x, y) = \iint A(f_x, f_y) \times \exp[j2\pi(f_x x + f_y y)] df_x df_y$ with $A(f_x, f_y) = A_0(f_x, f_y) \times \exp(jkz\sqrt{1-(\lambda f_x)^2 - (\lambda f_y)^2})$, where $k = 2\pi/\lambda$, $A_0(f_x, f_y) = F\{u_t(x, y)\}$, $F\{\cdot\}$ denotes the Fourier transform, and $\mathbf{f} = [f_x, f_y]$ represents a spatial frequency encoded in the MCAL. The propagation direction of the diffracted waves can be expressed as $d = [\lambda f_x, \lambda f_y, \sqrt{1 - (\lambda f_x)^2 - (\lambda f_y)^2}]^T$. When the diffracted waves are projected on plane $Z = 1$, the coordinates of the image intensity can be expressed as $[p_x, p_y, 1]^T = [\frac{x}{Z}, \frac{y}{Z}, 1]^T$, where $[p_x, p_y]^T$ denotes the position of the image intensity's centroid. Based on the geometric imaging relationship of optical cameras, the position of the image points on the image plane can be expressed as $[p_u, p_v, 1] = [f \ 0 \ u_0; 0 \ f \ v_0; 0 \ 0 \ 1][p_x, p_y, 1]^T$, where f is the focal length and (u_0, v_0) is the position of the principal point. In fact, the pinhole-imaging model does not include lens distortion of the optical system. When considering optical distortion in a camera system, the actual position of the image point on an image plane is expressed as $[p'_x, p'_y]^T = [p_x, p_y]^T + \Delta(x, y)$, where $\Delta(x, y)$ is the positional error of the image point due to optical distortions. The optical distortion of optical cameras can result from multiple factors such as design errors, machining errors, and assembly errors. All these factors can produce deviations of the image point from the ideal position on the image plane. The distortion of camera systems is modeled in the following expression $\Delta x = p_x(k_1 r^2 + k_2 r^4 + k_3 r^6 + \dots)$, $\Delta y = p_y(k_1 r^2 + k_2 r^4 + k_3 r^6 + \dots)$, where $r^2 = p_x^2 + p_y^2$, and k_1 , k_2 , and k_3 are distortion parameters. Therefore, the actual position of the image point on the image plane is calculated by the following equation $[\hat{p}_u, \hat{p}_v]^T = [u_0, v_0]^T + f[p_x, p_y]^T(1 + k_1 r^2 + k_2 r^4 + k_3 r^6 + \dots)$. When we attempt to use multiple points to perform an inverse calculation to solve the IOP, multiple equations similar to Eq. 9 can be obtained. With the aforementioned distortion features, the total minimum distortion in the full FOV of a camera can be attained at the principal distance and principal point. Based on the positional relationship of m image points, the internal parameters, i.e., principal distance and principal points, can be inverted using a minimized cost function as follows:

$$\min_m \left\| \begin{bmatrix} p_u - u_0, p_v - v_0 \\ + f [p_x \ p_y]^T (1 + k_1 r^2 + k_2 r^4 + k_3 r^6 + \dots) \end{bmatrix} \right\|_2^2. \quad (1)$$

Based on Eq. 1, f , u_0 , and v_0 can be calculated.

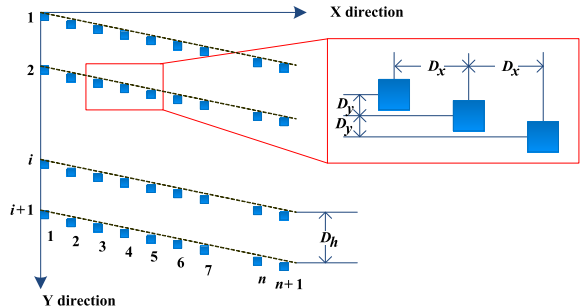


Fig. 2. MCAL design pattern.

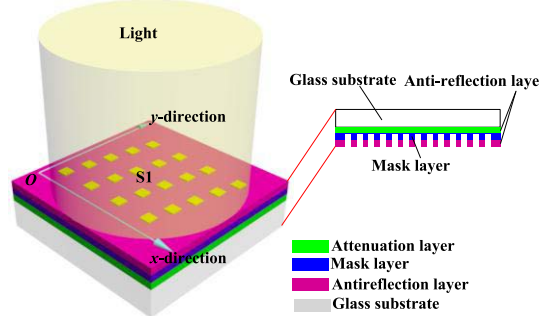


Fig. 3. Structure of MCAL, where S1 denotes one of the apertures.

To obtain spots over the entire camera sensor area, the maximum diffraction angle of the MCAL must generally be greater than the FOV of the camera. Each of the diffracted beams is focused within the image of the camera. In general, a remote sensing camera scans the image. Its image sensor adopts a time-delay integration (TDI) imaging mechanism. Based on this, the aperture of the MCAL is periodically encoded, as indicated in Fig. 2. The separation distance in the x -direction and y -direction is D_x and D_y , respectively, where $D_h = n \times D_y$, where n denotes the aperture number of each line. The spatial frequencies are given by $f_x = \gamma_x/\eta_x$ and $f_y = \gamma_y/\eta_y$, where γ_x denotes the diffraction order and η_x is the parameter determined by the period of the MCAL.

Fig. 3 displays the laminated structure of the MCAL, which is composed of four layers: attenuation layer, mask layer, antireflection layer, and glass substrate. Previous fabrication processes were different as they used an erosion method [6]; a secondary-development method based on surface micromachining is used to fabricate the CAL in this work. Fig. 4 illustrates the fabrication process of the CAL. Step 1, a layer of chromium film is plated on the glass substrate to attenuate the light. This layer does not form the aperture pattern. Step 2, the photoresist is spread evenly onto the plated substrate. Step 3, proximity lithography exposes the photoresist through a photomask. Step 4, the first development is performed to remove the exposed photoresist to form the preliminary pattern. Step 5, a layer of aluminum film is plated on the preliminary pattern.

The aluminum film is called a mask layer because it can selectively allow part of lights to pass through based on the pattern. Step 6, a second chromium layer is plated on the aluminum film to prevent secondary reflection. Finally, in Step 7, a second development is performed to remove the

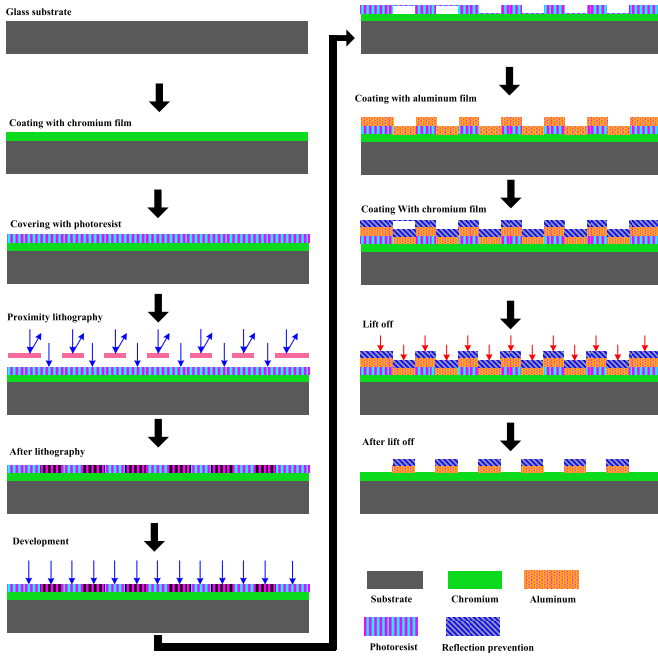


Fig. 4. Surface micromachining process for MCAL fabrication.

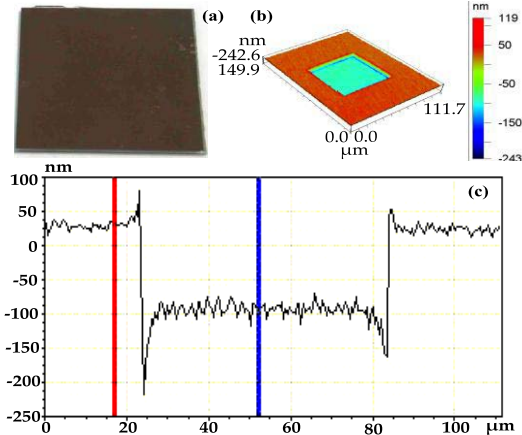


Fig. 5. (a) MCAL; (b) 3D morphology profile of single aperture; and (c) 2D profile of single aperture.

unexposed photoresist that remains after the first development. This implements the desired pattern on the plated substrate. In this step, the aluminum and chromium films covering the photoresist are also removed. The developer removes the unexposed photoresist. This process is also called lift-off, which means the photoresist and attached metal films are removed from the mask. After this step, the encoded apertures are formed. Light can pass through the lift-off apertures, whereas other parts block the incoming light.

III. CALIBRATING CAMERA

We experimentally demonstrate calibrating one camera using MCAL. Fig. 5 displays the fabricated sample. A sketch of the experimental calibration system is displayed in Fig. 6. The system includes an optical camera, MCAL, camera controller, collimator, camera, vapor-floating platform, ground testing devices, and remote control. The collimator can produce infinite plane waves for the test system. The output beam size of the collimator is greater than three times the size of the period in the MCAL; that is $D \geq 3 \times m \times \lambda / \sin \alpha$, where α is

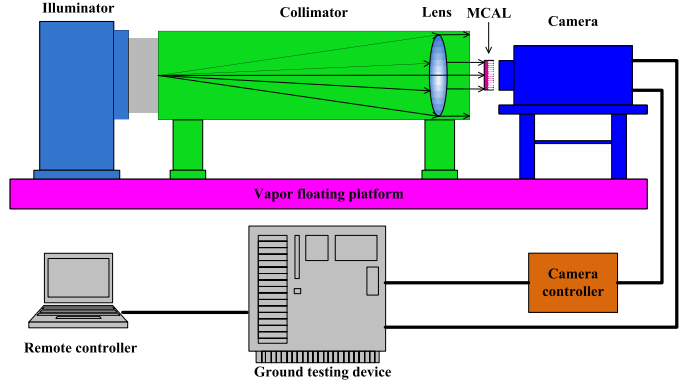


Fig. 6. Experimental system.

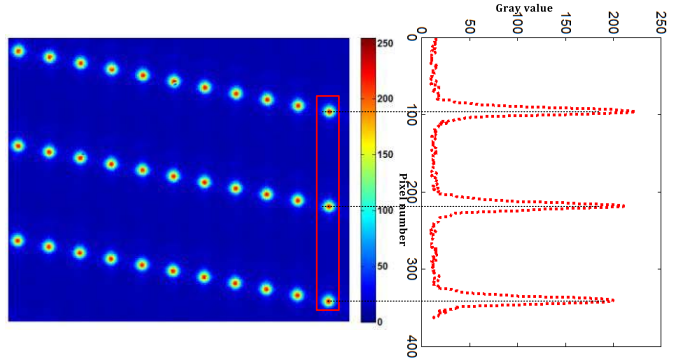


Fig. 7. Image of MCAL.

TABLE I
PARAMETERS OF UNCALIBRATED CAMERA

Number	Value
Aperture diameter	102.6mm
F/ratio	10
Focal length	1026mm
FOV	1°
Image resolution	1280 × 1024 pixels

the angle between the diffracted beam of order m and the optical axis, m is the diffraction order, and λ is the wavelength. In the optical system, a Co-axial Schmidt–Cassegrain (CSC) structure is used and a CMOS detector is used as the image sensor of the uncalibrated camera. The main parameters of the camera are presented in Table I. The wavelength range of the remote sensing camera is 500–800 nm. The central wavelength is 600 nm. The illuminator is an LED light source with central wavelength of 600 nm.

When the remote controller sends a calibration command to the camera controller through the ground-testing device, the camera begins capturing an image. The captured images are displayed in Fig. 7. As the displayed image's multiple encoded points are obtained, the internal parameters of the uncalibrated camera are inverted. In the proposed method, we use the mathematical morphology (MM)-based spot centroid algorithm to determine the position of each image point. Based on the position information of the multiple image points obtained using Eq. 9, the IOP of the uncalibrated camera can be inverted. We compared the proposed method with the ground-based calibration method, which is based on measuring angles [8]. Table II lists the calculated results for the internal parameters of the experimental camera using the two different methods. As displayed in Table II, the principal

TABLE II
COMPARISON RESULTS OF INTERNAL PARAMETERS OF EXPERIMENTAL
CAMERA USING TWO DIFFERENT METHODS

Number	Elements	Calibration value
Proposed method	f (mm)	1026.61
	U0x (mm)	0.4891
	U0y (mm)	0.5832
Reference method	f (mm)	1026.69
	U0x (mm)	0.5181
	U0y (mm)	0.6062

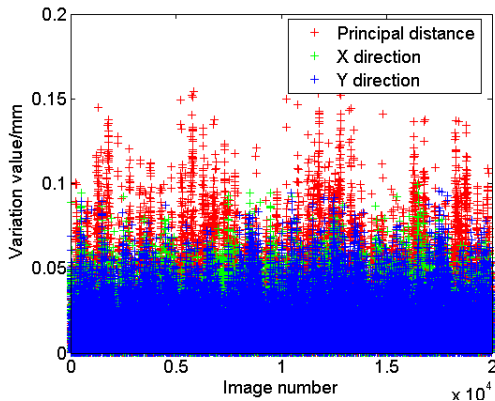


Fig. 8. Variation of principal distance and principal point.

distance evaluated by the proposed method, was 1026.61 mm, whereas for the ground reference method (GRM) [8]–[11], it was 1026.69 mm. The deviation between the two methods was 0.08 mm. The measured deviation between the two methods can mainly be attributed to the GRM's turntable vibration error and turntable angular control and measurement error, as well as the errors encountered in both methods, such as image point extraction error, system adjustment error, environmental vibrations, and airflows. However, the deviations between the two methods are acceptable because the calibration error of the internal parameters of the camera was less than 0.1 mm. This calibration error was obtained using an error allocation based on the measurement of the error of the external parameters such as attitude error and orbital error.

IV. DISCUSSION AND CONCLUSION

We also tested the calibration accuracy of the proposed method. Several devices such as gas-floating vibration isolation platforms and constant temperature controllers were used to build an experimental environment with minimum disturbance. Tens of thousands of images were used to invert the IOPs of the camera. The variation of the principal point and principal distance is indicated in Fig. 8.

We used a mean square error formula to assess the calibration accuracy of the proposed method. The calibration accuracy of the principal distance was $\delta_f = 3\delta = 0.0735$ mm. The calibration accuracy of the principal point reached $\delta_x = 3\delta = 0.0723$ and $\delta_y = 3\delta = 0.045$ mm in the x and y directions, respectively. The sensitivity of the reference method was influenced primarily by factors related to the turntable, vibration, assembly of the calibration configurations, extraction algorithm of the centroid position, light sources, fabricated parameter of the single pixel target, and calibration environment. The sensitivity of the proposed method was mainly influenced

by factors related to the assembly of the MCAL, extraction algorithm of the centroid position, fabricated parameters (D_x , D_y , D_h) of the MCAL, laser wavelength, and single aperture geometry. The extraction accuracy of the two methods approached 0.1 pixels, which means the extraction error was 0.6 μm when the pixel size was 6 μm . The parameters of the MCAL and other calibration configurations of the two methods were accurately measured and calibrated via high-accuracy auxiliary devices. When the calibration environments and measurement accuracy of the system parameters were the same, the proposed method was not influenced by either the vibration or angle measurement of the rotating turntable. Moreover, the reference method only performed each imaging process to capture a single image point of 2D FOV. Multiple calibration operations will decrease the calibration accuracy. We also used other central wavelengths LEDs to calibrate the camera. The calibration deviation of the internal parameters remained at the aforementioned calibration accuracy.

In conclusion, we presented the concept of geometrically calibrating the IOPs of a remote sensing camera with MCAL and confirmed it experimentally. We believe that this principle can be used in the application of high accuracy image positioning of remote sensing cameras in combination with high efficient imaging methods [12]. In the future, the following methods could be altered to improve the calibration accuracy. First, a light diffraction model of the MCAL could be established. Further, the design of the MCAL could be optimized. Finally, an image-position-extraction algorithm with a higher accuracy, such as a correlation-matching algorithm, could replace the current method.

REFERENCES

- [1] C. S. Fraser and M. Ravanbakhsh, "Georeferencing from Geoeye-1 imagery: Early indications of metric performance," in *Proc. Int. Soc. Photogramm. Remote Sens. Hannover Workshop*, vol. 6. 2009, pp. 1–6.
- [2] J. Li, Y. Zhang, S. Liu, and Z. Wang, "Self-calibration method based on surface micromachining of light transceiver focal plane for optical camera," *Remote Sens.*, vol. 8, no. 11, pp. 893–914, 2016.
- [3] J. Li, F. Xing, T. Sun, Z. Liu, and Z. You, "Space high-accuracy intelligence payload system with integrated attitude and position determination," *Instrumentation*, vol. 2, no. 1, pp. 3–16, 2015.
- [4] T. A. Clarke and J. F. Fryer, "The development of camera calibration methods and models," *Photogramm. Rec.*, vol. 16, pp. 51–66, Apr. 1998.
- [5] R. Fu, Y. Zhang, and J. Zhang, "Study on geometric measurement methods for line-array stereo mapping camera," *Spacecraft Recovery Remote Sens.*, vol. 32, pp. 62–67, Oct. 2011.
- [6] J. Li, F. Xing, D. Chu, and Z. Liu, "High-accuracy self-calibration for smart optical orbiting payloads integrated with attitude and position determination," *Sensors*, vol. 16, no. 8, pp. 1176–1196, 2016.
- [7] J. Hieronymus, "Comparison of methods for geometric camera calibration," in *Proc. 22nd ISPRS Congr. Int. Arch. Photogramm., Remote Sens. Spatial Inf. Sci.*, vol. 39. 2012, pp. 595–599.
- [8] F. Yuan, W. J. Qi, and A. P. Fang, "Laboratory geometric calibration of areal digital aerial camera," in *Proc. IOP Conf. Ser., Earth Environ. Sci.*, vol. 17. 2014, p. 012196.
- [9] R. Schuster and B. Braunecker, "The calibration of the ADC (airborne digital camera)—System," *Int. Arch. Photogramm. Remote Sens.*, vol. 33, pp. 288–294, Jul. 2000.
- [10] T. Chen, R. Shibasaki, and Z. Lin, "A rigorous laboratory calibration method for interior orientation of an airborne linear push-broom camera," *Photogramm. Eng. Remote Sens.*, vol. 73, no. 4, pp. 369–374, 2007.
- [11] G.-D. Wu, B. Han, and X. He, "Calibration of geometric parameters of line-array CCD camera based on exact measuring angle in lab," *Opt. Precis. Eng.*, vol. 15, no. 10, pp. 1628–1632, 2007.
- [12] J. Li, Z. Liu, and F. Liu, "Compressive sampling based on frequency saliency for remote sensing imaging," *Sci. Rep.*, vol. 7, p. 6539, Jul. 2017.